Measurement of Cosmic-Ray Proton and Antiproton Spectra at Mountain Altitude

T. Sanuki [a,*], M. Fujikawa [a], H. Matsunaga [a,1], K. Abe [b], K. Anraku [a,2], H. Fuke [a], S. Haino [a], M. Imori [a], K. Izumi [a], T. Maeno [b,3], Y. Makida [c], N. Matsui [a], H. Matsumoto [a], J. Nishimura [a], M. Nozaki [b], S. Orito [a,4], M. Sasaki [c,5], Y. Shikaze [b], J. Suzuki [c], K. Tanaka [c], A. Yamamoto [c], Y. Yamamoto [a], K. Yamato [b], T. Yoshida [c], and K. Yoshimura [c]

[a] *The University of Tokyo, Bunkyo, Tokyo 113-0033, Japan*

[b] *Kobe University, Kobe, Hyogo 657-8501, Japan*

[c] *High Energy Accelerator Research Organization (KEK), Tsukuba, Ibaraki 305-0801, Japan*

Abstract

Cosmic-ray proton and antiproton spectra were measured at mountain altitude, 2770 m above sea level. We observed more than 2×10^5 protons and 10^2 antiprotons in a kinetic energy range between 0.25 and 3.3 GeV. The zenith-angle dependence of proton flux was obtained. The observed spectra were compared with theoretical predictions.

Key words: atmospheric cosmic ray, cosmic-ray proton, cosmic-ray antiproton, superconducting spectrometer
PACS: 13.85.Tp, 95.85.Ry

* Corresponding author.
Email address: sanuki@phys.s.u-tokyo.ac.jp (T. Sanuki).

[1] Present address: University of Tsukuba, Tsukuba, Ibaraki 305-8571, Japan
[2] Present address: Kanagawa University, Yokohama, Kanagawa 221-8686, Japan
[3] Present address: CERN, CH-1211 Geneva 23, Switzerland
[4] deceased.
[5] Present address: National Aeronautics and Space Administration, Goddard Space Flight Center, Greenbelt, MD 20771, USA

1 Introduction

Primary cosmic rays hit the Earth's atmosphere and produce baryons and mesons via hadronic interactions. Absolute fluxes of these secondary cosmic rays at any altitudes can be calculated based on primary cosmic-ray intensity and interaction cross sections. Observations of the secondary cosmic rays are very important for understanding the production and propagation of secondary cosmic-ray particles inside the atmosphere. It will provide information to verify or to improve the theoretical models. A number of experiments for measuring primary cosmic rays have been carried out at balloon altitude or in space, and atmospheric muons on the ground as well as under the ground. A long-period observation at mountain altitude with high statistics will provide a good reference for a study of secondary cosmic-ray particles inside the atmosphere.

Only a few measurements of cosmic-ray proton fluxes at mountain altitude were reported [1,2,3,4]. Antiproton flux at mountain altitude was also reported [4] previous to this work. The reported flux was quite higher than theoretical predictions.

We report here a new observation of cosmic-ray protons and antiprotons at mountain altitude in a kinetic energy range between 0.25 and 3.3 GeV. A spectral shape of cosmic-ray antiprotons at mountain altitude was measured for the first time. These data will provide essentially important information about hadronic interactions between cosmic rays and atomic nuclei inside the atmosphere.

2 BESS Experiment

2.1 Detector

The BESS (Balloon-borne Experiment with a Superconducting Spectrometer) detector [5,6,7,8,9,10] is a high-resolution spectrometer with a large acceptance to perform highly sensitive searches for rare cosmic-ray components, as well as precise measurement of the absolute fluxes of various cosmic rays. Fig. 1 shows a schematic cross-sectional view of the BESS instrument. In the central region, a uniform magnetic field of 1 Tesla is provided by using a thin superconducting solenoidal coil. A magnetic-rigidity ($R \equiv Pc/Ze$) of an incoming charged particle is measured by a tracking system, which consists of a jet-type drift chamber (JET) and two inner-drift-chambers (IDC's) inside the magnetic field. The deflection (R^{-1}) and its error are calculated for each event

by applying a circular fitting using up to 28 hit points, each with a spatial resolution of 200 μm. The maximum detectable rigidity (MDR) was estimated to be 200 GV. Time-of-flight (TOF) hodoscopes provide the velocity (β) and energy loss ($\mathrm{d}E/\mathrm{d}x$) measurement. A $1/\beta$ resolution of 1.6 % was achieved in this experiment. In order to separate protons and antiprotons from muons, the BESS spectrometer is equipped with a threshold-type aerogel Čerenkov counter. The refractive index of silica aerogel radiator is 1.022, which corresponds to a threshold kinetic energy of 3.6 GeV for protons and antiprotons. Each particle is identified by requiring proper $1/\beta$, as well as $\mathrm{d}E/\mathrm{d}x$, as a function of the rigidity.

There are a plastic scintillating counter, an acrylic Čerenkov counter and a lead plate just above the bottom TOF hodoscope. The lead plate covers about 1/5 of the total acceptance. These counters were used for electron/muon identification in the muon analysis [11]. In the analysis of protons and antiprotons discussed here, the signals from these counters were not examined.

All detector components are arranged in a cylindrical configuration. This simple configuration and the uniform magnetic field result in a large geometrical acceptance and uniform performance in momentum measurement.

A simple coincidence of the top- and bottom-TOF hodoscope signals issues the first-level "T0-trigger." The live data-taking time is measured exactly by counting 1 MHz clock pulses with a scaler system gated by a "ready" status that controls the T0-trigger.

2.2 Observations

The atmospheric cosmic-ray events were observed at Norikura Observatory, ICRR, the University of Tokyo, Japan. It is located at $36^\circ\ 06'N, 137^\circ\ 33'E$. The altitude is 2,770 m above sea level. The vertical geomagnetic cutoff rigidity is 11.2 GV [12].

The observation was performed during two periods of 17th – 19th and 21st – 23rd of September 1999. During the observation, the atmospheric depth and temperature varied as shown in Fig. 2. The mean (root-mean-square) atmospheric depth and temperature were 742.4 (2.9) g/cm^2 and 10.9 (1.1) °C, respectively. The BESS detector was operated outside the building and in a nylon plastic sheet tent so as to be less influenced by ambient conditions. There was no thick material within a field of view of the detector. A gas flow system was implemented to keep the purity and pressure of the gas inside the chambers stable enough for operation.

The T0-trigger rate was about 50 Hz. It is much lower than that at a usual

balloon floating altitude of about 37 km. Thus, all events which satisfied the T0-trigger condition were recorded without imposing second-level trigger nor on-line rejections. This simple trigger condition reduced systematic errors. The live-time ratio was as high as 98.8 % through the observation. The number of collected events was about 2.0×10^7.

3 Data analysis

Particle mass was reconstructed by the velocity, rigidity and charge for each event, and was required to be consistent with a proton and an antiproton. Fig. 3 shows $1/\beta$ distribution as a function of rigidity after requiring that there was no light output from the aerogel Čerenkov counter, so as to discriminate protons and antiprotons from muons.

The procedure of data analysis was almost the same as that of the balloon-flight data [13,14,15] except for a method of evaluating the performance of the aerogel Čerenkov counter. The cosmic rays at the balloon altitude are dominated by protons. On the other hand, those at mountain altitude consist almost of muons. Therefore the efficiency of the aerogel Čerenkov counter for protons and antiprotons was not obtained from the observed data in this analysis. The efficiency and its dependence on particle's velocity were estimated by using muons in a lower rigidity range of $|R| < 1.7$ GV, where muons were identified without contaminations. The obtained efficiency was applied to protons and antiprotons. This process arose an additional systematic error of 4 %. In a higher rigidity range of $|R| > 1.7$ GV, protons and antiprotons were contaminated by muons. The number of contaminating muons was estimated by multiplying the total number of observed particles by the probability that a muon fakes a proton or an antiproton. The fake probability was evaluated to be 10^{-4} by using energetic particles above 10 GeV and the same muon sample as was used for estimating the efficiency of the aerogel Čerenkov counter. The muon background amounted to about 20 % for the antiprotons above 2 GeV. It was negligibly small for the protons.

In this analysis, the zenith angle (θ_z) was limited as $\cos\theta_z \geq 0.95$ for protons. Because of the very small flux of antiprotons, the lower limit of $\cos\theta_z$ for antiproton analysis was relaxed to be 0.84 so as to improve its statistics.

4 Results and discussion

The observed energy spectra of protons and antiprotons are shown in Figs. 4 and 5, respectively, together with previous measurements at mountain altitude

[1,2,3,4] and theoretical predictions [16,17,18,19]. Tables 1 and 2 summarize the obtained spectra. The first and second errors in Tables 1 and 2 represent statistical and systematic errors, respectively. Since the statistics of antiproton measurement was very limited, the statistical error was calculated as a 68.7 % confidence interval based on a "unified approach" [20].

4.1 Protons

There is some difference among the proton fluxes observed by various experiments as shown in Fig. 4. Table 3 summarizes the locations of cosmic-ray observations at mountain altitude. According to our simple Monte Carlo simulations, the difference was generally explained by the different altitudes and cutoff rigidities. The overall spectral shape is reproduced by theoretical calculations [16,19].

Fig. 6 shows the zenith angle dependence of the observed proton flux, $F(\cos\theta_z)$, in two kinetic energy regions. In a simple one-dimensional approximation, the zenith angle dependence can be expected as

$$F(\cos\theta_z) = F_0 \exp\left(\frac{X}{\Lambda}\left(1 - \frac{1}{\cos\theta_z}\right)\right), \tag{1}$$

where X is the atmospheric depth at the observation site and Λ is the attenuation length of protons inside the atmosphere. The dashed lines in Fig. 6 show the expectation, in which $X/\Lambda = 6$ was assumed, since the atmospheric depth was 742.4 g/cm^2 and the proton attenuation length is about 120 g/cm^2. Normalization was done by tuning F_0 so that the total flux, $2\pi \int F(\cos\theta)\cos\theta d\cos\theta$, is equal to the observed total flux. Relatively good agreement is found between the observed data and the expectation in the higher energy region. In the lower energy region, however, much larger deviation is observed in the zenith angle dependence. These facts are most likely due to the effect of angular spread of secondary protons produced via nuclear interactions. This "three-dimensional effect" was evaluated by a simple analytic method considering the distribution of transverse momentum at the production point of secondary protons. The solid lines shown in Fig. 6 give the results of the analytic calculation, in which the angular spread was taken into account. They reproduce the observed data in the whole energy range better than the expectation by the one-dimensional calculation.

As mentioned above, the proton flux shown in Fig. 4 was obtained by using the events satisfying the zenith angle condition of $\cos\theta_z \geq 0.95$. The average zenith angle, $\langle\cos\theta_z\rangle$, was 0.98. The vertical flux $F_0 \equiv F(\cos\theta_z \rightarrow 1)$ was obtained by fitting the observed fluxes using a formula (1), where "X/Λ" was

used as a fitting parameter. The F_0 obtained by fitting the data in $\cos\theta_z \geq 0.95$ is summarized in the last column of Table 1. The systematic error due to this fitting procedure was estimated to be around 5 % by checking variations of F_0 in changing the fitting regions.

4.2 Antiprotons

Fig. 5 shows that the obtained antiproton spectrum above 1 GeV is generally consistent with theoretical predictions obtained through transport equation calculations by Bowen and Moats [16] and Stephens [17], as well as through a three-dimensional Monte Carlo simulation by Huang et al. [18]. In the lower energy region, however, the transport equation calculations show significant disagreement with our results. Those three calculations predict similar antiproton spectrum above 0.3 GeV at a thin residual atmosphere of 5 g/cm^2, but their predictions do not agree so well with each other at mountain altitude [16,17,18]. It means that the shapes of antiproton production spectra are very similar to each other, and that the difference at mountain altitude is to be made mainly due to the different treatment of the propagation inside the atmosphere. The production spectrum of antiprotons has a sharp peak around 2 GeV [17]. The flux at 0.5 GeV is as small as 1/10 of the peak flux. Therefore most antiprotons observed below 1 GeV are tertiary antiprotons, those which have been produced inside the atmosphere and then lost their energy during the propagation inside the atmosphere. In this case, interaction processes of $\bar{p} + A$ (nuclei) have to be precisely treated for an accurate evaluation of antiproton spectrum at mountain altitude. In the calculation of Refs. [16,17], the probability that an antiproton with initial energy of E_0 possesses energy E after a collision was assumed to be uniform from $E = 0$ to $E = 0.90E_0$ or $0.95E_0$. On this assumption, the average energy after a collision is about a half of the initial energy. In the calculation of Ref. [18], on the other hand, only annihilation channels were taken into account in the inelastic interactions. Non-annihilating inelastic processes were not included as a process of antiproton energy loss, thus a tertiary antiproton remains as energetic as before the interaction. Our result suggests that the non-annihilation process does not make significant contribution to the inelastic interactions of antiprotons during their propagation inside the atmosphere. Thus, the antiprotons are considered not to lose their energy considerably in the non-annihilating inelastic processes.

The antiproton flux measured by Sembroski et al. [4] is much higher than our measurements in spite of the similar observational conditions such as altitude (Table 3). In that experiment, a particle trajectory was measured with six chambers only outside the magnetic field. No information about the particle trajectory was obtained inside the magnetic field. It might lead to some

difficulty in strict identification of antiprotons.

5 Summary

We have measured proton and antiproton spectra in a kinetic energy range of 0.25 – 3.5 GeV at Mt. Norikura, 2,770 m above sea level, in Japan. The vertical geomagnetic cutoff rigidity is 11.2 GV. The mean atmospheric depth during the measurement was 742.4 g/cm^2.

The measured proton spectrum is consistent with the previous results, if the different altitudes and cutoff rigidities at their observation sites are taken into account. The zenith angle dependence of the proton flux was observed. It suggests importance of a three-dimensional effect of the angular spread in secondary baryon productions especially in a low energy region.

The measured antiproton flux above 1 GeV generally agrees with the theoretical predictions. In the lower energy region, however, our flux shows much better agreement with the calculation performed in assuming that tertiary antiprotons remain as energetic as before interactions. Our result suggests that the energy loss of antiprotons due to non-annihilation process is not significant during their propagation inside the atmosphere.

Acknowledgements

This study was supported by a Joint Research Program of ICRR, the University of Tokyo. We would like to thank all staffs at the Norikura Observatory for their cooperation and helpful suggestions. We are indebted to Professor M. Buénerd and Professor L. Derome of Laboratoire de Physique Subatomique et de Cosmologie, IN2P3/CNRS and Dr. C. Y. Huang of Max-Planck-Institut für Kernphysik for helpful discussions on this issue. We would like to thank KEK and ICEPP, the University of Tokyo for their continuous support and encouragement during this study. This experiment was supported by Grants-in-Aid, KAKENHI(11694104, 11440085, 09304033), from Ministry of Education, Culture, Sports, Science and Technology, MEXT, and Japan Society for the Promotion of Science, JSPS, in Japan.

References

[1] K. M. Kocharian, Sov. Phys. JETP 1 (1955) 128.

[2] K. M. Kocharian et al., Sov. Phys. JETP 35 (1959) 933.

[3] H. B. Barber et al., Phys. Rev. D22 (1980) 2667.

[4] G. H. Sembroski et al., Phys. Rev. D33 (1986) 639.

[5] S. Orito, in: Proc. ASTROMAG Workshop, KEK Report KEK87-19 (1987) 111.

[6] A. Yamamoto et al., Adv. Space Res. 14 (1994) 75.

[7] Y. Asaoka et al., Nucl. Instrum. Meth. A416 (1998) 236.

[8] Y. Ajima et al., Nucl. Instrum. Meth. A443 (2000) 71.

[9] Y. Shikaze et al., Nucl. Instrum. Meth. A455 (2000) 596.

[10] Y. Asaoka et al., Nucl. Instrum. Meth. A489 (2002) 170.

[11] T. Sanuki et al., Phys. Lett. B541 (2002) 234.

[12] M. A. Shea and D. F. Smart, Proc. 27th ICRC(Hamburg) (2001) 4063.

[13] S. Orito et al., Phys. Rev. Lett. 84 (2000) 1078.

[14] T. Maeno et al., Astropart. Phys. 16 (2001) 121.

[15] Y. Asaoka et al., Phys. Rev. Lett. 88 (2002) 051101.

[16] T. Bowen and A. Moats, Phys. Rev. D33 (1986) 651.

[17] S. A. Stephens, Astropart. Phys. 6 (1997) 229.

[18] C. Y. Huang et al., astro-ph/0305367 (2003), submitted to Phys. Rev. D, and private communication.

[19] B. Baret et al., astro-ph/0305369 (2003), submitted to Phys. Rev. D, and private communication.

[20] G. J. Feldman and R. D. Cousins, Phys. Rev. D57 (1998) 3873.

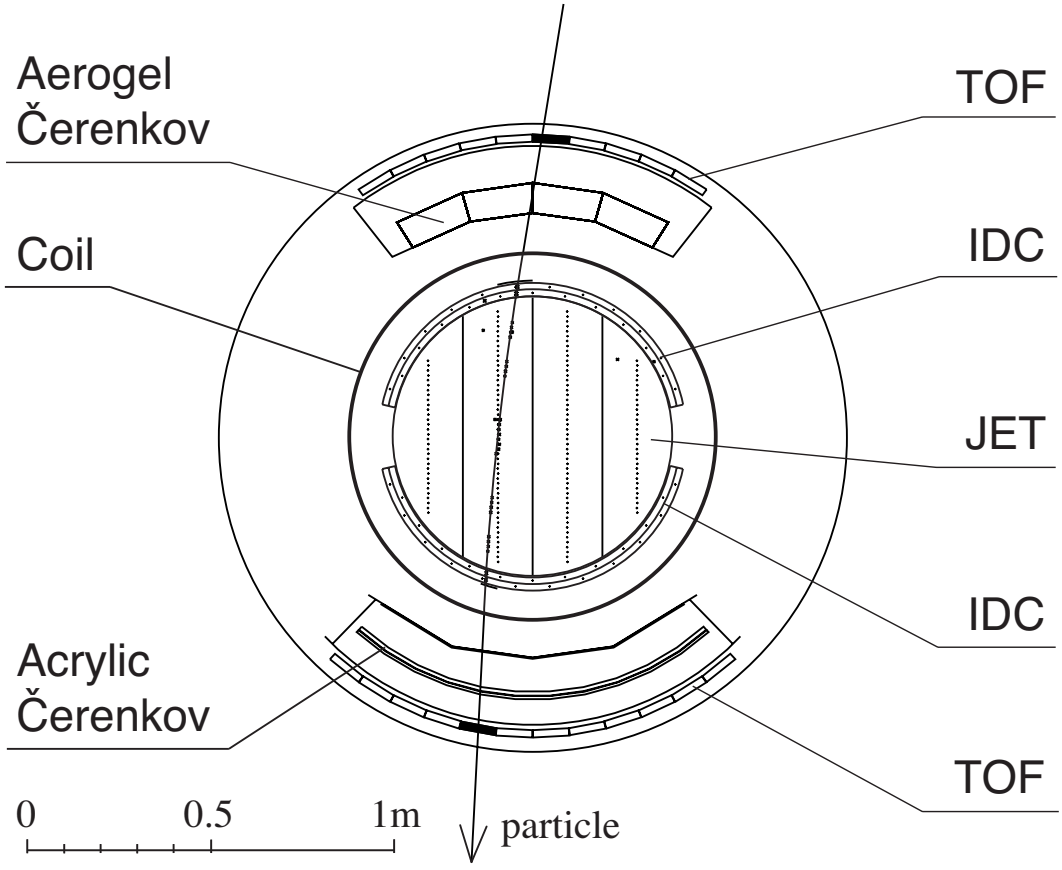

Fig. 1. Schematic cross-sectional view of the BESS detector.

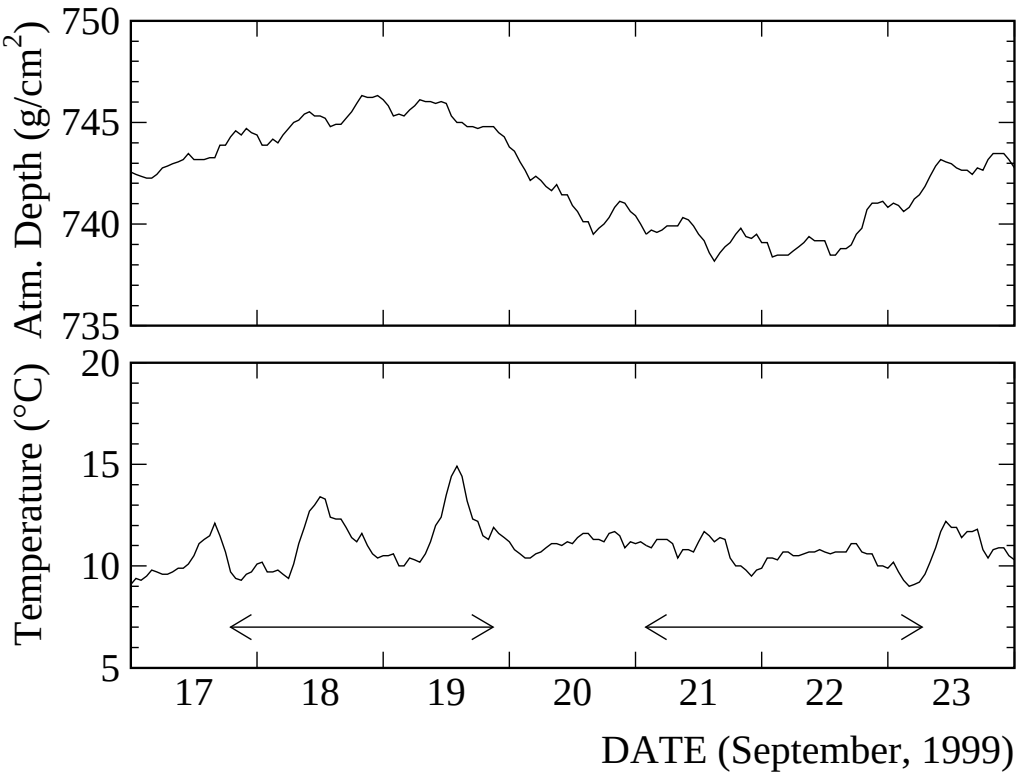

Fig. 2. Atmospheric depth and temperature during the observation. The experiment was performed during two periods of 17th – 19th and 21st – 23rd.

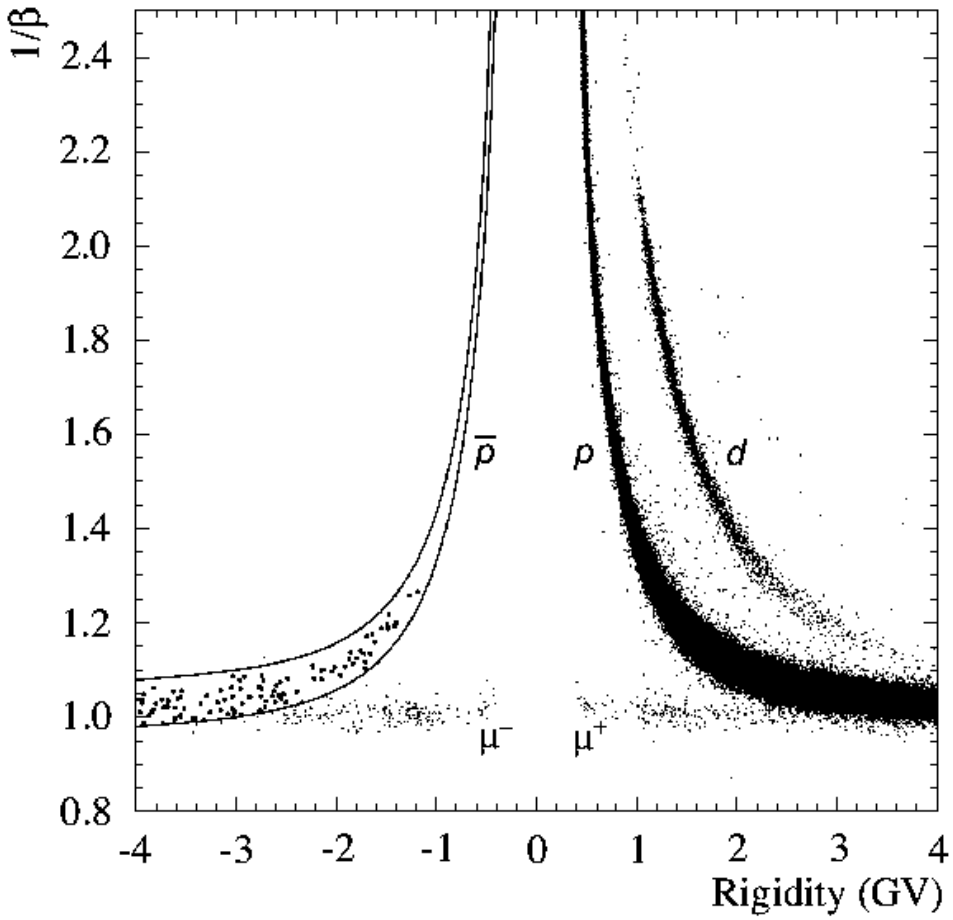

Fig. 3. Identification of antiproton events. The solid lines define the antiproton selection band.

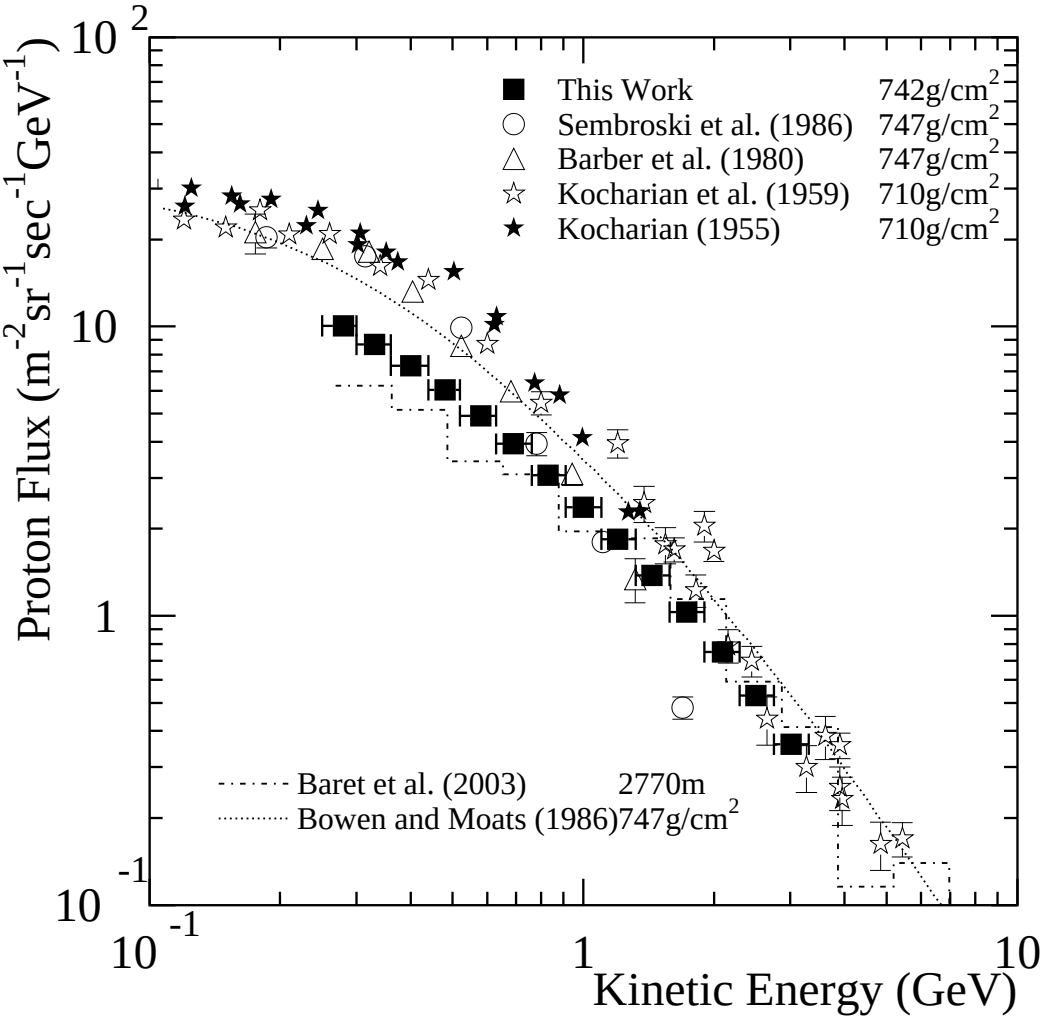

Fig. 4. The observed proton spectrum compared with the previous works, and with the theoretical calculations.

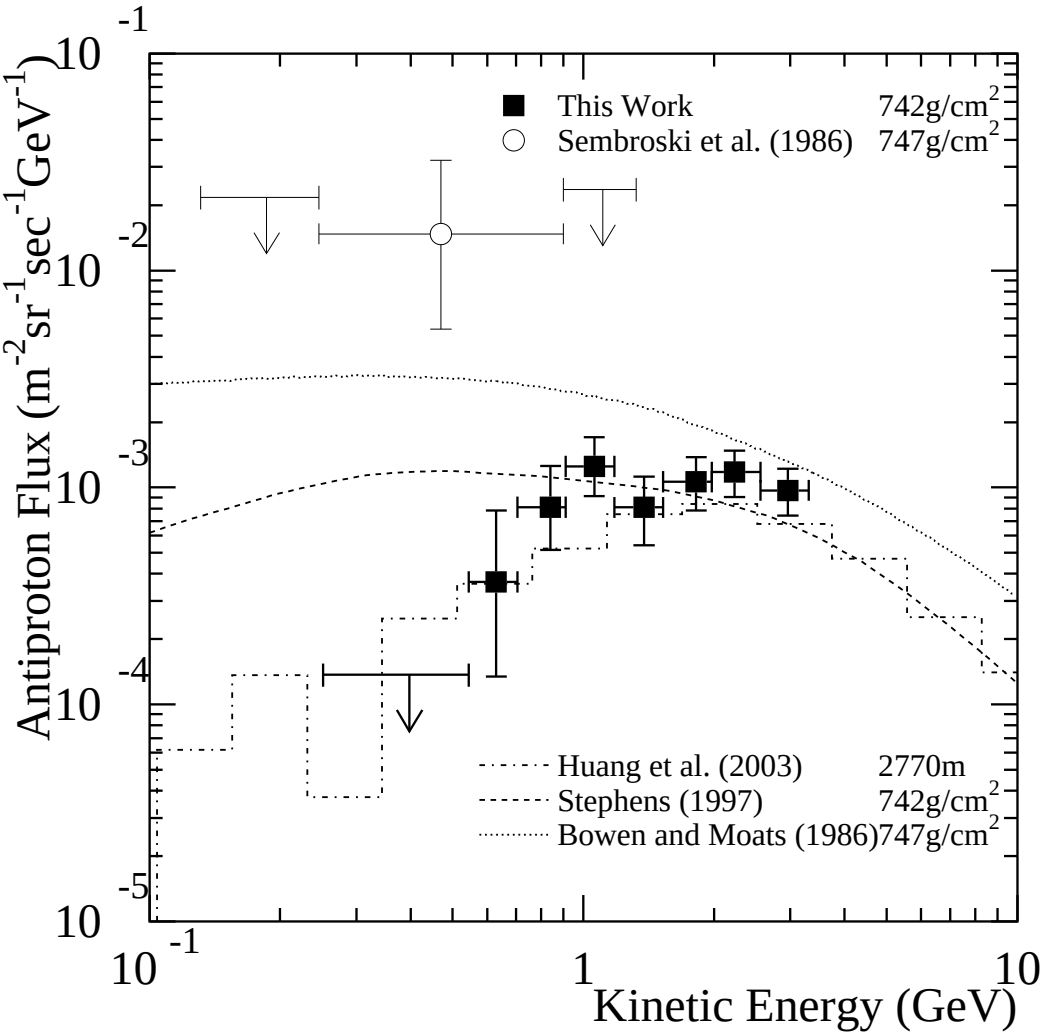

Fig. 5. The observed antiproton spectrum compared with the previous works, and with the theoretical calculations. The dashed line was reproduced by interpolating between two spectra at 700 g/cm^2 and 900 g/cm^2 using a power law.

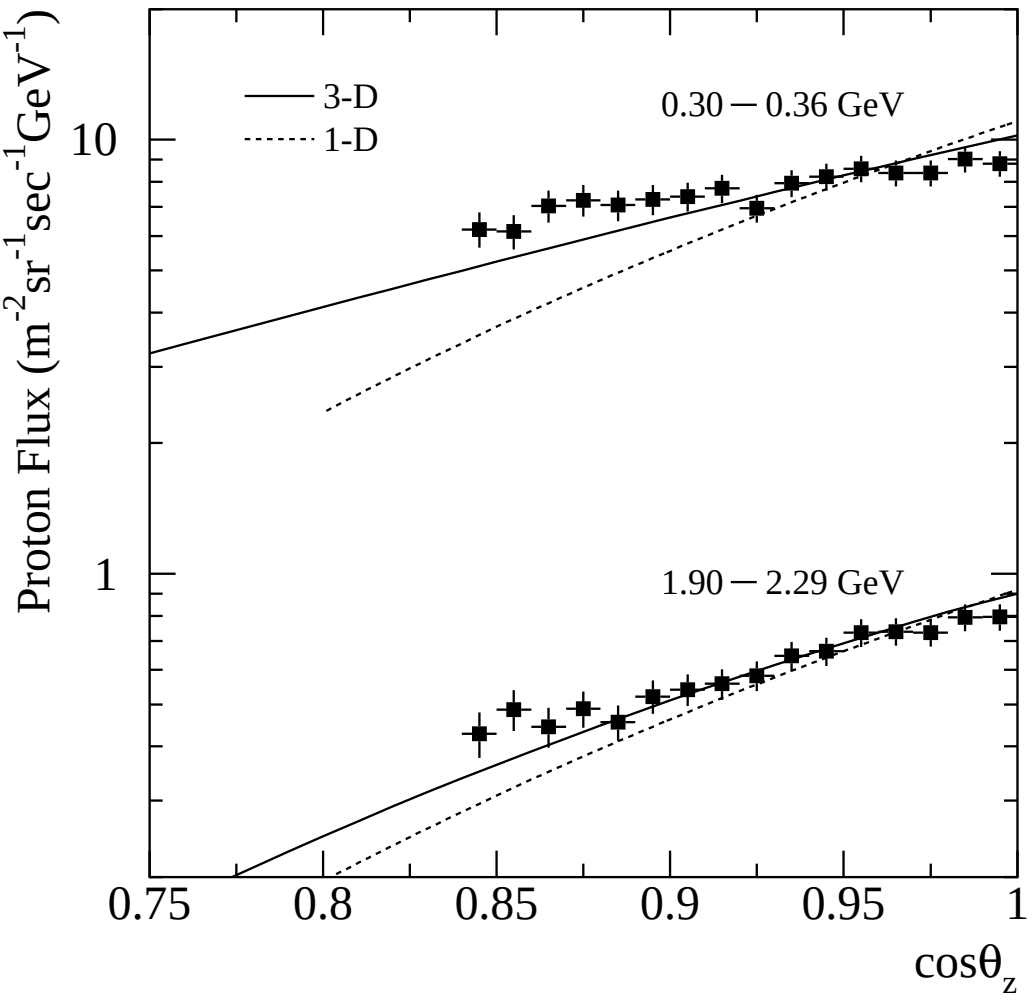

Fig. 6. The zenith angle dependence of proton flux. The dotted and solid lines show the expected dependence in simple one-dimensional and three-dimensional calculations, respectively.

Table 1
Observed spectrum of protons.

Kinetic Energy		Number of p's	$\langle\cos\theta_z\rangle$	Proton Flux	
Range (GeV)	Mean (GeV)			$\cos\theta_z \geq 0.95$	$\cos\theta_z \to 1$
				$(\mathrm{m}^{-2}\mathrm{sr}^{-1}\mathrm{sec}^{-1}\mathrm{GeV}^{-1})$	
0.25 – 0.30	0.28	10528	0.98	$10.05 \pm 0.10 \pm 0.46$	$10.70 \pm 0.10 \pm 0.73$
0.30 – 0.36	0.33	11472	0.98	$8.66 \pm 0.08 \pm 0.40$	$8.89 \pm 0.08 \pm 0.61$
0.36 – 0.44	0.40	12048	0.98	$7.33 \pm 0.07 \pm 0.34$	$7.81 \pm 0.07 \pm 0.53$
0.44 – 0.52	0.48	12219	0.98	$6.04 \pm 0.05 \pm 0.28$	$6.26 \pm 0.06 \pm 0.43$
0.52 – 0.63	0.58	12014	0.98	$4.91 \pm 0.04 \pm 0.23$	$5.16 \pm 0.05 \pm 0.35$
0.63 – 0.76	0.69	11487	0.98	$3.93 \pm 0.04 \pm 0.18$	$4.17 \pm 0.04 \pm 0.28$
0.76 – 0.91	0.83	10711	0.98	$3.06 \pm 0.03 \pm 0.14$	$3.21 \pm 0.03 \pm 0.22$
0.91 – 1.10	1.00	9664	0.98	$2.37 \pm 0.02 \pm 0.12$	$2.52 \pm 0.03 \pm 0.18$
1.10 – 1.32	1.20	8889	0.98	$1.84 \pm 0.02 \pm 0.09$	$1.94 \pm 0.02 \pm 0.14$
1.32 – 1.58	1.44	7803	0.98	$1.38 \pm 0.02 \pm 0.07$	$1.47 \pm 0.02 \pm 0.11$
1.58 – 1.90	1.73	6877	0.98	$1.03 \pm 0.01 \pm 0.05$	$1.07 \pm 0.01 \pm 0.08$
1.90 – 2.29	2.09	5947	0.98	$0.75 \pm 0.01 \pm 0.04$	$0.80 \pm 0.01 \pm 0.06$
2.29 – 2.75	2.50	4940	0.98	$0.53 \pm 0.01 \pm 0.03$	$0.57 \pm 0.01 \pm 0.04$
2.75 – 3.31	3.01	4026	0.98	$0.36 \pm 0.01 \pm 0.02$	$0.39 \pm 0.01 \pm 0.03$

Table 2
Observed spectrum of antiprotons.

Kinetic Energy		Number of $\bar{p}$'s	Number of BG's	$\langle\cos\theta_z\rangle$	Antiproton Flux
Range (GeV)	Mean (GeV)				$\cos\theta_z \geq 0.84$ ($m^{-2}sr^{-1}sec^{-1}GeV^{-1}$)
0.25 – 0.54	–	0	0.0	–	1.37×10^{-4} upper limit
0.54 – 0.70	0.63	2	0.0	0.97	$3.67^{+4.14+0.17}_{-2.32-0.17} \times 10^{-4}$
0.70 – 0.91	0.84	6	0.0	0.97	$8.11^{+4.44+0.38}_{-2.94-0.38} \times 10^{-4}$
0.91 – 1.18	1.06	12	0.0	0.94	$1.25^{+0.45+0.08}_{-0.33-0.08} \times 10^{-3}$
1.18 – 1.53	1.38	10	0.1	0.96	$8.09^{+3.10+0.53}_{-2.62-0.53} \times 10^{-4}$
1.53 – 1.98	1.82	18	1.3	0.96	$1.06^{+0.31+0.07}_{-0.27-0.07} \times 10^{-3}$
1.98 – 2.56	2.23	29	5.2	0.96	$1.18^{+0.29+0.08}_{-0.26-0.08} \times 10^{-3}$
2.56 – 3.31	2.96	33	7.8	0.94	$9.70^{+2.43+0.63}_{-2.18-0.63} \times 10^{-4}$

Table 3
Summary of the observation sites at mountain altitude.

	This Work	Refs. [1,2]	Refs. [3,4]
Site	Mt. Norikura	Mt. Aragats	Mt. Lemmon
Altitude	2770 m	3200 m	2750 m
Atmospheric Depth	742 g/cm^2	710 g/cm^2	747 g/cm^2
Cutoff Rigidity	11.2 GV	7.6 GV	5.6 GV